DTIC FILE COPY

AD-A198 680

MARYLAND

COLLEGE PARK CAMPUS

A Backprojection Algorithm for Electrical Impedance Imaging

Fadil Santosa

Department of Mathematical Sciences
University of Delaware
Newark, DE 19716

and

Michael Vogelius

Department of Mathematics
and
Institute for Physical Science and Technology
University of Maryland
College Park, MD 20742

DTIC
ELECTE
AUG 1 5 1988
S D
H

Technical Note BN-1081

July 1988

INSTITUTE FOR PHYSICAL SCIENCE AND TECHNOLOGY

DISTRIBUTION STATEMENT A
Approved for public release;
Distribution Unlimited

88 5 ..

Encl (1)

SECURITY CLASSIFICATION OF THIS PAGE (When Data Entered)

REPORT DOCUMENTATION PAGE

READ INSTRUCTIONS BEFORE COMPLETING FORM

1. REPORT NUMBER: BN-1081

2. GOVT ACCESSION NO.:

3. RECIPIENT'S CATALOG NUMBER:

4. TITLE (and Subtitle): A Backprojection Algorithm for Electrical Impedance Imaging

5. TYPE OF REPORT & PERIOD COVERED: Final life of the contract

6. PERFORMING ORG. REPORT NUMBER:

7. AUTHOR(s): Fadil Santosa[1] and Michael Vogelius[2]

8. CONTRACT OR GRANT NUMBER(s): [1]ONR N-00014-85-K0725, NSF DMS-8720428; [2]NSF DMS-8601490, ONR N-00014-85-K0169

9. PERFORMING ORGANIZATION NAME AND ADDRESS:
[1]Depart. of Math. Sciences, University of Delaware, Newark, DE 19716
[2]Depart. of Math. & Inst. for Physical Science and Technology, University of MD, College Park, MD 20742

10. PROGRAM ELEMENT, PROJECT, TASK AREA & WORK UNIT NUMBERS:

11. CONTROLLING OFFICE NAME AND ADDRESS:
Department of the Navy, Office of Naval Research, Arlington, VA 22217

12. REPORT DATE: July 1988

13. NUMBER OF PAGES: 33

14. MONITORING AGENCY NAME & ADDRESS (if different from Controlling Office):

15. SECURITY CLASS. (of this report):

15a. DECLASSIFICATION/DOWNGRADING SCHEDULE:

16. DISTRIBUTION STATEMENT (of this Report):

Approved for public release: distribution unlimited

17. DISTRIBUTION STATEMENT (of the abstract entered in Block 20, if different from Report):

18. SUPPLEMENTARY NOTES:

19. KEY WORDS (Continue on reverse side if necessary and identify by block number):

20. ABSTRACT (Continue on reverse side if necessary and identify by block number):

We study a two-dimensional reconstruction algorithm due to D.C. Barber and B.H. Brown, applied to a linearized electrostatic inverse problem. Firstly we demonstrate how this algorithm fits within the framework of inverses of generalized Radon transforms studied by G. Beylkin. Secondly we construct an iterative improvement of the Barber-Brown algorithm based on the conjugate residual method. We present several numerical results obtained with this iterative algorithm.

DD FORM 1 JAN 73 1473 EDITION OF 1 NOV 65 IS OBSOLETE

S/N 0102-LF-014-6601

SECURITY CLASSIFICATION OF THIS PAGE (When Data Entered)

A backprojection algorithm for electrical impedance imaging

Fadil Santosa*
Department of Mathematical Sciences
University of Delaware
Newark, DE 19716

and

Michael Vogelius†
Department of Mathematics
University of Maryland
College Park, MD 20742

May, 1988

Abstract

We study a two-dimensional reconstruction algorithm due to D.C. Barber and B.H. Brown, applied to a linearized electrostatic inverse problem. Firstly we demonstrate how this algorithm fits within the framework of inverses of generalized Radon transforms studied by G. Beylkin. Secondly we construct an iterative improvement of the Barber-Brown algorithm based on the conjugate residual method. We present several numerical results obtained with this iterative algorithm.

1 Introduction

In electrical impedance imaging one seeks to reconstruct the internal conductivity (or impedance) profile of an object from boundary measurements of voltages and corresponding current fluxes. There has been significant advances made in recent years on both practical aspects of the reconstruction problem [2, 3, 11, 16, 17] as well as on theoretical aspects of the uniqueness and continuous dependence question [1, 10, 14, 15, 18]. We shall not attempt a review of the literature; the reader may consult [6] for an extensive list of references.

One particular algorithm which has shown itself to be surprisingly effective given its low cost was developed by D.C. Barber and B.H. Brown [2, 3] for use in the context of medical tomography. In this paper we analyze the Barber and Brown method in some detail. In particular we show that the crucial backprojection component of the algorithm

*Research partly supported by ONR contract N-00014-85-K0725 and NSF-AFOSR grant DMS-8720428

†Research partly supported by ONR contract N-00014-85-K0169, NSF grant DMS-8601490 and the Sloan Foundation

may simply be viewed as part of an approximate inverse of a generalized Radon transform, as studied extensively by Beylkin [4, 5].

The Barber and Brown algorithm has already been compared numerically to several other algorithms [19] and appears quite exceptional in achieving a moderate accuracy at an extremely low cost. In the latter part of this paper we construct an iterative extension of Barber and Brown's algorithm based on a conjugate residual method. This new algorithm can achieve a significantly higher accuracy at a modest increase in computational cost.

In the analysis and computations of this paper, we restrict ourselves to a circular domain and consider only the linearized identification problem. We are currently in the process of implementing the iterative algorithm for the full nonlinear problem on an arbitrary polygonal domain. Results from this work will be reported elsewhere.

The paper is organized into seven sections. In Section 2, we give a brief description of the electrical impedance problem, and review Barber and Brown's backprojection scheme. In Section 3 we show how the Barber and Brown backprojection fits within the framework of approximate inverses of generalized Radon transforms, constructed by Beylkin. We also examine the relation between the linearized elliptic forward problem and a generalized Radon transform. Section 4 provides a discussion of our implementation of the Barber-Brown algorithm. In Section 5 we study properties of the conductivity-to-data map and its composition with the backprojection; in particular, we perform an eigenvalue analysis to study the sensitivity of these maps. This study leads to the development of an iterative algorithm based on a conjugate residual method, as presented in Section 6. Results from our numerical experimentations with the iterative method are displayed in Section 7.

2 The linearized inverse problem–A backprojection reconstruction

As a mathematical model for the direct current electrostatic problem, we suppose

$$\begin{aligned} \nabla \cdot (\gamma \nabla u) &= 0 \quad \text{in} \quad \Omega \\ \gamma \frac{\partial u}{\partial n} &= \psi \quad \text{on} \quad \partial\Omega, \end{aligned} \tag{1}$$

where u is the voltage potential, ψ is a boundary current, and γ denotes the conductivity profile. The linearized problem for a small perturbation $\delta\gamma$ (of γ) and corresponding perturbation δU (of U) now becomes

$$\begin{aligned} \nabla \cdot (\gamma \nabla \delta U) &= -\nabla \cdot (\delta\gamma \nabla U) \quad \text{in} \quad \Omega, \\ \gamma \frac{\partial(\delta U)}{\partial n} &= -\delta\gamma \frac{\partial U}{\partial n} \quad \text{on} \quad \partial\Omega. \end{aligned}$$

In the remainder of this paper, we shall for simplicity assume that

(i) Ω is the unit ball, $\Omega = \{x \in I\!R^2 : |x| < 1\}$.

(ii) $\gamma \equiv 1$.

We take U to be a dipole solution, more specifically U solves

$$\begin{aligned} \Delta U &= 0 \quad \text{in} \quad \Omega, \\ \frac{\partial U}{\partial n} &= -\pi \frac{\partial}{\partial \tau} \delta_\omega \quad \text{on} \quad \partial\Omega, \end{aligned} \tag{2}$$

INSPECTED 2
sion For
GRA&I
TAB
unced
ication
Distribution/
Availability Codes
Dist | Avail and/or Special
A-1

where $\partial\delta_\omega/\partial\tau$ is the counter clockwise tangential derivative of a Dirac delta-function, δ_ω, $\omega \in \partial\Omega$. We furthermore assume that

(iii) $\delta\gamma = 0$ near the dipole.

Under assumptions (ii) and (iii) the linearized problem reduces to

$$\begin{aligned} \Delta\delta U &= -\nabla(\delta\gamma)\cdot\nabla U \quad \text{in} \quad \Omega, \\ \frac{\partial(\delta U)}{\partial n} &= 0 \quad \text{on} \quad \partial\Omega. \end{aligned} \tag{3}$$

The original problem in electrical impedance imaging is to determine a consistent γ, given knowledge of $u|_{\partial\Omega}$ (the solution to (1)) for various choices of ψ. The linearized inverse problem associated with (3) therefore becomes

(I P) *Given $\delta U|_{\partial\Omega}$ for various choices of dipole solution U, determine a consistent increment $\delta\gamma$.*

We use the notion consistent, since of course none of these inverse problems can be expected to have a unique solution given only a limited set of choices of boundary fluxes. The algorithm of Barber and Brown represents an ingenious one step approximate solution to the problem (I P). To explain the algorithm we briefly review its derivation (along the lines of [3]).

Since Ω is the unit ball, the solution to (2) is known in closed form:

$$U = \frac{x_1'}{x_1'^2 + x_2'^2} \quad \text{with} \quad x_1' = \omega^\perp \cdot x, \quad x_2' = 1 - \omega\cdot x,$$

where $\omega^\perp = (-\omega_2, \omega_1)$ is the $\pi/2$ rotate of the dipole location $\omega = (\omega_1, \omega_2)$. The function

$$V = \frac{x_2'}{x_1'^2 + x_2'^2}$$

is a harmonic conjugate to U on Ω. Indeed, $x \to (U, V)$ (the so-called Poincaré map) conformally maps Ω onto the upper half plane $P = \{V > 1/2\}$. The problem (3) simplifies in the (U, V) coordinates to read

$$\begin{aligned} \Delta\delta U &= -\frac{\partial(\delta\gamma)}{\partial U} \quad \text{in} \quad P \\ \frac{\partial(\delta U)}{\partial V} &= 0 \quad \text{on} \quad \partial P = \{V = 1/2\}. \end{aligned} \tag{4}$$

Note that the function $\delta\gamma = \delta\gamma(x(U, V, \omega))$ is now a function of U, V and ω. The extra data being used to reconstruct $\delta\gamma$ is the function $\delta U|_{V=1/2}$ (a function of U and ω). For a single fixed dipole location ω_0, a consistent conductivity increment $\delta\gamma_0$ is given by

$$\delta\gamma_0(x) = -\frac{\partial}{\partial U}(\delta U|_{V=1/2})(U(x, \omega_0), \omega_0),$$

as follows easily from (4). Barber and Brown suggest the average

$$\tilde{B}(x) = -\frac{1}{2\pi}\int_{|\omega|=1} (\frac{\partial}{\partial U}\delta U|_{V=1/2})(s, \omega)|_{s=U(x,\omega)}\Phi(x, \omega)dS_\omega, \tag{5}$$

as a rough approximation to the conductivity increment $\delta\gamma$ ($\tilde{B}$ is of course not in general consistent with any dipole measurements).

The formula (5) has a geometrical interpretation illustrated by Figure 1. Given a point x to be imaged, and a dipole location ω, consider the equipotential circular arc $\{z : U(z,\omega) = U(x,\omega) = s\}$ which originates at ω and passes through x. The point where this equipotential arc intersects the boundary is $x(s, 1/2, \omega)$ (in U, V coordinates, for fixed ω, it corresponds to $U = s, V = 1/2$). The first term in the integrand is the known quantity $(\frac{\partial}{\partial\tau}\delta U/\frac{\partial}{\partial\tau}U)(x(s,1/2,\omega),\omega)$ (see (6) below).

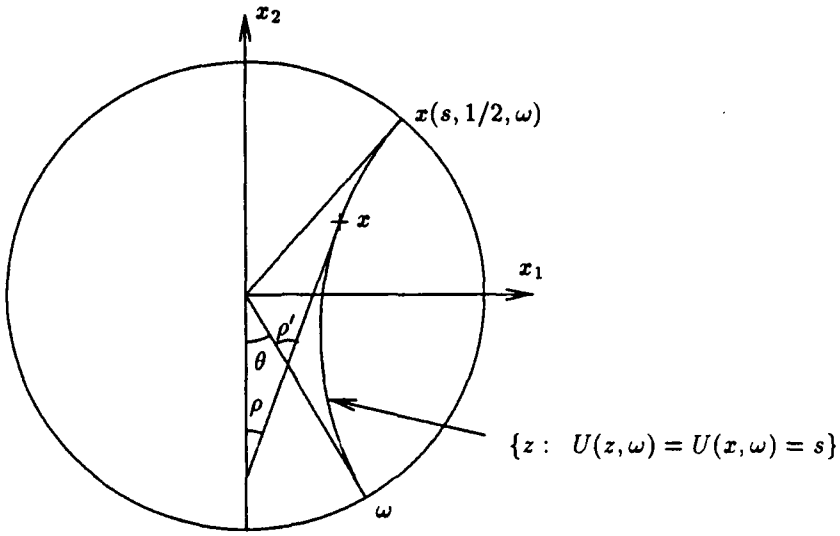

Figure 1 In this picture, the dipole is located at ω, the equipotential arc through x is displayed. The intersection of the equipotential arc with the boundary is $x(s, 1/2, \omega)$.

The weight Φ is selected in a very particular fashion. Let ρ be the angle between the tangent to the curve $U(z,\omega) = U(x,\omega)$ at x and the vector $(0,1)$. Denote by θ the angle between $(0,-1)$ and ω (cf. Figure 1). The function $\Phi(x,\omega)$ equals $|\partial\rho/\partial\theta(x,\omega)|$, so that

$$\Phi(x,\omega)dS_\omega = |\frac{\partial\rho}{\partial\theta}(x,\omega)|d\theta = d\rho,$$

(for a fixed imaging point x). Therefore, the average in (5) is exactly

$$-\frac{1}{2\pi}\int_0^{2\pi}(\frac{\partial}{\partial U}\delta U|_{V=1/2})(s,\omega)|_{s=U(x,\omega)}d\rho,$$

which corresponds to a uniform distribution of angle ρ (not θ).

It is not difficult to see that

$$\Phi(x,\omega) = 2V(x,\omega) - 1 \tag{6a}$$

and

$$(\frac{\partial}{\partial U}\delta U|_{V=1/2})(s,\omega) = (\frac{\partial}{\partial\tau}\delta U/\frac{\partial}{\partial\tau}U)(x(s,1/2,\omega),\omega). \tag{6b}$$

Indeed, in Figure 1, $\rho = \rho' - \theta$ and so

$$\frac{\partial\rho}{\partial\theta} = \frac{\partial\rho'}{\partial\theta} - 1.$$

On the other hand in the x' coordinates (for fixed ω) the tangent to the curve $\{z : U(z,\omega) = U(x,\omega)\}$ is

$$\frac{(\nabla_{x'}U)^\perp}{|\nabla_{x'}U|} = \begin{pmatrix} 2x_1'x_2' \\ x_2'^2 - x_1'^2 \end{pmatrix} / (x_1'^2 + x_2'^2)$$

and therefore

$$\cos\rho' = \frac{x_2'^2 - x_1'^2}{x_1'^2 + x_2'^2} \quad , \quad \sin\rho' = \frac{2x_1'x_2'}{x_1'^2 + x_2'^2}. \tag{7}$$

Differentiation of the first formula in (7) yields

$$\frac{\partial\rho'}{\partial\theta} = -\frac{\partial}{\partial\theta}\left(\frac{x_2'^2 - x_1'^2}{x_1'^2 + x_2'^2}\right) / \sin\rho' = -\frac{\partial}{\partial\theta}\left(\frac{x_2'^2 - x_1'^2}{x_1'^2 + x_2'^2}\right)\frac{x_1'^2 + x_2'^2}{2x_1'x_2'},$$

and a simple computation, using

$$\frac{\partial}{\partial\theta}x_1' = x_2' - 1, \quad \frac{\partial}{\partial\theta}x_2' = -x_1',$$

now gives

$$\frac{\partial\rho'}{\partial\theta} = 2 - 2V.$$

Consequently

$$\frac{\partial\rho}{\partial\theta} = 1 - 2V(x,\omega),$$

which immediately leads to the formula (6a).

The formula (6b) represents a simple change of variable, since

$$(\frac{\partial}{\partial U}\delta U|_{V=1/2})(s,\omega) = \frac{\nabla_{x'}\delta U \cdot \nabla_{x'}U}{|\nabla_{x'}U|^2}(x(s,1/2,\omega),\omega) = (\frac{\partial}{\partial\tau}\delta U / \frac{\partial}{\partial\tau}U)(x(s,1/2,\omega),\omega),$$

where $\partial/\partial\tau$ is the counter clockwise tangential derivative and $x(s,1/2,\omega)$ is as in Figure 1.

The Barber and Brown average may now be written

$$\tilde{B}(x) = \frac{1}{2\pi}\int_{|\omega|=1}(\frac{\partial}{\partial\tau}\delta U / \frac{\partial}{\partial\tau}U)(x(s,1/2,\omega),\omega)|_{s=U(x,\omega)}(1 - 2V(x,\omega))dS_\omega. \tag{8}$$

Except for a filter, which we shall briefly discuss later, the calculation of the integrals (8) represent exactly the reconstruction method suggested by Barber and Brown. In the following section, we explain how (8) may be seen as part of an approximate inverse for a generalized Radon transform.

3 The generalized Radon transform and its inverse

The function

$$\phi(x,\xi) = |\xi|\, U(x,\xi/|\xi|), \quad x \in \Omega, \quad \xi \in I\!R^2 \setminus \{0\}.$$

is positive-homogeneous of degree one:

$$\phi(x,\lambda\xi) = \lambda\phi(x,\xi), \quad \lambda \in I\!R_+, \tag{9}$$

it is also infinitely often differentiable in $\Omega \times (I\!R^2 \setminus \{0\})$ and

$$\nabla_x\phi(x,\xi) \neq 0 \quad \forall x \in \Omega, \xi \in I\!R^2 \setminus \{0\}. \tag{10}$$

The function ϕ defines a family of arcs (parts of circles) to be used for the generalized Radon transform

$$H_{s,\omega} = \{x \in \Omega : \phi(x,\omega) = s\}, \quad s \in I\!R, \quad |\omega| = 1.$$

As a measure on each arc $H_{s,\omega}$ we take

$$d\mu = |\nabla_x \phi|^{-1} d\sigma,$$

where $d\sigma$ denotes standard arclength; we let a denote the amplitude

$$a(x,\omega) = |\nabla_x \phi(x,\omega)|^2. \tag{11}$$

Following the notation in [4] we now define a generalized Radon transform

$$\begin{aligned} (Ru)(s,\omega) &= \int_{H_{s,\omega}} u(x) a(x,\omega) d\mu \\ &= \int_{H_{s,\omega}} u(x) |\nabla_x \phi(x,\omega)| d\sigma \end{aligned} \tag{12}$$

for any $u \in C_0^\infty(\Omega)$.

Beylkin provides a recipe for the approximate inversion of transforms like that in (12). His main assertion is that

$$R^\star K R = id + T, \tag{13}$$

where T is compact: $L^2(\Omega, compact) \to L^2(\Omega, loc)$ and $R^\star$ is the so-called backprojection

$$(R^\star v)(x) = \int_{|\omega|=1} \frac{h(x,\omega)}{a(x,\omega)} v(s,\omega)|_{s=\phi(x,\omega)} dS_\omega. \tag{14}$$

K consists in convolution with the generalized kernel

$$k(s) = \frac{1}{2(2\pi)^2} \int_{-\infty}^{\infty} |r| e^{irs} dr. \tag{15}$$

The function h is given by

$$h(x,\xi) = det(\frac{\partial^2 \phi(x,\xi)}{\partial x_j \partial \xi_k}).$$

The weight $h(x,\omega)/a(x,\omega), |\omega| = 1$, appearing in $R^\star$ has a very simple relation to $|\partial\rho/\partial\theta| = 2V - 1$ (cf. Figure 1).

Lemma 1

$$h(x,\omega)/a(x,\omega) = 2V(x,\omega) - 1, \quad x \in \Omega, \quad |\omega| = 1.$$

Proof

Using polar coordinates (r_ξ, θ_ξ) in the ξ-plane, we get

$$\begin{aligned} h(x,\omega) &= [(\frac{\partial}{\partial \xi_1} \nabla_x \phi)^\perp \cdot (\frac{\partial}{\partial \xi_2} \nabla_x \phi)](x,\omega) \\ &= [(\frac{\partial}{\partial r_\xi} \nabla_x \phi)^\perp \cdot (\frac{\partial}{\partial \theta_\xi} \nabla_x \phi)](x,\omega) \end{aligned}$$

for $|\omega| = 1$. Since ϕ is positive-homogeneous of degree 1 and since θ_ξ is the same as the angle θ (corresponding to $\omega = \xi/|\xi|$ in Figure 1) we get

$$h(x,\omega) = [(\nabla_x \phi)^\perp \cdot (\frac{\partial}{\partial \theta} \nabla_x \phi)](x,\omega). \tag{16}$$

Note that the formula (16) only involves the function $\phi(x,\omega)$, $|\omega| = 1$, due to the fact that differentiations with respect to θ and x are performed with $r_\xi = |\xi| = constant = 1$.

As before, let x' denote the coordinates related to x by the orthogonal affine transformation

$$x' = Q_\theta x + \begin{pmatrix} 0 \\ 1 \end{pmatrix}, \quad \text{where} \quad Q_\theta = \begin{pmatrix} \omega^\perp \\ -\omega \end{pmatrix} = \begin{pmatrix} \cos\theta & \sin\theta \\ -\sin\theta & \cos\theta \end{pmatrix}.$$

Then $\nabla_x = Q_\theta^T \nabla_{x'}$, and from (16) we therefore get

$$\begin{aligned} h(x,\omega) &= (Q_\theta^T \nabla_{x'}\phi)^\perp \cdot ((\frac{\partial}{\partial\theta} Q_\theta)^T \nabla_{x'}\phi) + (\nabla_{x'}\phi)^\perp \cdot (\frac{\partial}{\partial\theta}\nabla_{x'}\phi) \\ &= |\nabla_{x'}\phi|^2 + (\nabla_{x'}\phi)^\perp \cdot (\frac{\partial}{\partial\theta}\nabla_{x'}\phi). \end{aligned} \tag{17}$$

Division by $a = |\nabla_x \phi|^2 = |\nabla_{x'}\phi|^2$ yields

$$\frac{h(x,\omega)}{a(x,\omega)} = 1 + \left[\frac{(\nabla_{x'}\phi)^\perp}{|\nabla_{x'}\phi|} \cdot \frac{(\frac{\partial}{\partial\theta}\nabla_{x'}\phi)}{|\nabla_{x'}\phi|} \right](x,\omega). \tag{18}$$

The function ϕ satisfies

$$\phi(x,\omega) = \frac{x_1'}{x_1'^2 + x_2'^2},$$

and $\partial x_1'/\partial\theta = x_2' - 1, \partial x_2'/\partial\theta = -x_1'$. A simple calculation based on (18) now leads to

$$\begin{aligned} h(x,\omega)/a(x,\omega) &= 2\frac{x_2'}{x_1'^2 + x_2'^2} - 1 \\ &= 2V(x,\omega) - 1. \end{aligned}$$

□

Remark 3.1

We note that in his paper [4], Beylkin assumes that the phase function ϕ is odd with respect to the variable ξ (he assumes that ϕ is not just positive-homogeneous, but homogeneous of degree one). The only place this is used in an essential way is in the calculation of the splitting of the Fourier Integral Operator F, on page 583. F is given by

$$Fu(y) = \int_{|\omega|=1} G(y,\omega) dS_\omega,$$

with

$$G(y,\omega) = \frac{1}{(2\pi)^2} \int_0^\infty \left(\int_\Omega e^{i\Psi(x,y,r\omega)} A(x,y,r\omega) u(x) dx \right) r dr,$$

and

$$\Psi(x,y,\xi) = \phi(x,\xi) - \phi(y,\xi), \quad A(x,y,\xi) = \frac{a(x,\frac{\xi}{|\xi|}) h(y,\xi)}{a(y,\frac{\xi}{|\xi|})}$$

If ϕ is not necessarily odd with respect to ξ, then a slightly different calculation gives

$$\begin{aligned} G(y,\omega) &= \frac{1}{(2\pi)^2} \int_0^\infty e^{-ir\phi(y,\omega)} \frac{h(y,\omega)}{a(y,\omega)} r dr \left(\int_\Omega e^{ir\phi(x,\omega)} a(x,\omega) u(x) dx \right) \\ &= \frac{1}{(2\pi)^2} \int_0^\infty e^{-ir\phi(y,\omega)} \frac{h(y,\omega)}{a(y,\omega)} r dr \left(\int_{-\infty}^\infty e^{irs} Ru(s,\omega) ds \right), \end{aligned}$$

and therefore

$$Re(G(y,\omega)) = \frac{1}{2} \frac{1}{(2\pi)^2} \int_{-\infty}^\infty e^{-ir\phi(y,\omega)} \frac{h(y,\omega)}{a(y,\omega)} |r| dr \left(\int_{-\infty}^\infty e^{irs} Ru(s,\omega) ds \right),$$

provided u is real. In other words

$$Re(G(y,\omega)) = \frac{h(y,\omega)}{a(y,\omega)} KR(u)(\phi(y,\omega)),$$

where K represents convolution with the generalized kernel

$$\frac{1}{2(2\pi)^2}\int_{-\infty}^{\infty} |r| e^{irs} dr.$$

The formula that corresponds to (3.3) on page 584 of [4] in this case becomes

$$Re(Fu(y)) = R^\star KR(u)(y), \tag{19}$$

provided u is real. There are no changes required to show that

$$F = id + T \tag{20}$$

where T is compact: $L^2(\Omega, comp) \to L^2(\Omega, loc)$. Based on (19) and (20) we immediately conclude that

$$R^\star KR = id + \tilde{T}$$

where $\tilde{T}$ is compact: $L^2(\Omega, comp) \to L^2(\Omega, loc)$. □

Let W denote the function

$$W(s,\omega) = -\frac{1}{2\pi}\left(\frac{\partial}{\partial\tau}\delta U / \frac{\partial}{\partial\tau} U\right)(x(s,1/2,\omega),\omega)$$

From Lemma 1 we immediately get

$$\begin{aligned}
&(R^\star W)(x) \\
&= \int_{|\omega|=1} h(x,\omega)/a(x,\omega) W(s,\omega)|_{s=\phi(x,\omega)} dS_\omega \\
&= \frac{1}{2\pi}\int_{|\omega|=1} \left(\frac{\partial}{\partial\tau}\delta U / \frac{\partial}{\partial\tau} U\right)(x(s,1/2,\omega),\omega)|_{s=U(x,\omega)}(1-2V(x,\omega)) dS_\omega.
\end{aligned}$$

We shall shortly verify that

$$W \approx KR(\delta\gamma) \quad (\text{ in a very crude sense}). \tag{21}$$

We therefore conclude that the Barber and Brown average

$$\begin{aligned}
\frac{1}{2\pi}\int_{|\omega|=1} \left(\frac{\partial}{\partial\tau}\delta U / \frac{\partial}{\partial\tau} U\right)(x(s,1/2,\omega),\omega)|_{s=U(x,\omega)}(1-2V(x,\omega)) dS_\omega &= R^\star W(x) \\
&\approx R^\star KR(\delta\gamma)(x) \\
&\approx \delta\gamma(x)
\end{aligned}$$

may be viewed as a crude first approximation to $\delta\gamma(x)$. We find it quite remarkable that Barber and Brown by purely heuristic arguments were able to find the "right" weight $(2V-1)$ for their backprojection.

We complete this section by showing (21). The function

$$G_{(U_0,V_0)}(U,V) = -\frac{1}{4\pi}\left(\frac{U-U_0}{(U-U_0)^2+(V-V_0)^2} + \frac{U-U_0}{(U-U_0)^2+(V+V_0-1)^2}\right),$$

$V_0 > 1/2$, solves

$$\begin{aligned}
\Delta G_{(U_0,V_0)} &= -\frac{\partial}{\partial U}\delta_{(U_0,V_0)} \quad \text{in} \quad P = I\!R \times (1/2,\infty) \\
\frac{\partial G_{(U_0,V_0)}}{\partial V} &= 0 \quad \text{on} \quad \partial P = \{V = 1/2\}.
\end{aligned}$$

It follows from this and (4) that

$$\delta U(U,V,\omega) = \int_{-\infty}^{\infty}\int_{1/2}^{\infty} G_{(U',V')}(U,V)\delta\gamma(U',V',\omega)dV'dU',$$

and consequently

$$\begin{aligned}
&-(\frac{\partial}{\partial U}\delta U|_{V=1/2})(s,\omega) \\
&= -\int_{-\infty}^{\infty}\int_{1/2}^{\infty}\frac{\partial}{\partial U}G_{(U',V')}(s,1/2)\delta\gamma(U',V',\omega)dV'dU' \\
&= \frac{1}{2\pi}\int_{-\infty}^{\infty}\int_{1/2}^{\infty}\frac{(1/2-V')^2-(s-U')^2}{[(s-U')^2+(1/2-V')^2]^2}\delta\gamma(U',V',\omega)dV'dU'. \qquad (22)
\end{aligned}$$

Fourier transformation of (22) with respect to s leads to

$$-(\frac{\partial}{\partial U}\delta U|_{V=1/2})^{\wedge}(r,\omega) = \frac{1}{2}|r|\int_{1/2}^{\infty} e^{-(V'-1/2)|r|}\delta\gamma^{\wedge}(r,V',\omega)dV'; \qquad (23)$$

here we have used the fact that

$$\left(\frac{q^2-U^2}{(q^2+U^2)^2}\right)^{\wedge}(r) = \int_{-\infty}^{\infty}\frac{q^2-U^2}{(q^2+U^2)^2}e^{-irU}dU = \pi|r|e^{-q|r|}, \quad q>0.$$

If we replace $e^{-(V'-1/2)|r|}$ by its value at $r=0$ (or $V'=1/2$) then (23) reads

$$-(\frac{\partial}{\partial U}\delta U|_{V=1/2})^{\wedge}(r,\omega) \approx \frac{1}{2}|r|\,(\int_{1/2}^{\infty}\delta\gamma(\cdot,V',\omega)dV')^{\wedge}(r),$$

or equivalently

$$-(\frac{\partial}{\partial U}\delta U|_{V=1/2})(s,\omega) \approx 2\pi K(\int_{1/2}^{\infty}\delta\gamma(\cdot,V',\omega)dV')(s), \qquad (24)$$

where K represents convolution with the generalized kernel

$$\frac{1}{2(2\pi)^2}\int_{-\infty}^{\infty}|r|e^{irs}dr.$$

According to (6) the left hand side in (24) is exactly

$$-(\frac{\partial}{\partial\tau}\delta U/\frac{\partial}{\partial\tau}U)(x(s,1/2,\omega),\omega),$$

and by a simple change of variables

$$\int_{1/2}^{\infty}\delta\gamma(s,V',\omega)dV' = \int_{H_{s,\omega}}\delta\gamma(x)|\nabla_x U(x,\omega)|d\sigma = R(\delta\gamma)(s,\omega).$$

Therefore

$$-\frac{1}{2\pi}(\frac{\partial}{\partial\tau}\delta U/\frac{\partial}{\partial\tau}U)(x(s,1/2,\omega),\omega) \approx KR(\delta\gamma)(s,\omega)$$

as stated in (21).

Remark 3.2

We note that the approximation (21) is best for smooth $\delta\gamma$ or $\delta\gamma$ whose "singularities" lie not too far from the boundary. For $\delta\gamma$ with "singularities" near the center (21) represents only a very crude approximation. In contrast the approximation $R^*KR(\delta\gamma) \approx \delta\gamma$ seeks to fit "singularities" and represents only a very crude approximation for smooth $\delta\gamma$. This difference in the nature of the approximations, we believe, is the main reason that the Barber-Brown backprojection, R^*W, in itself only gives a crude approximation to $\delta\gamma$. □

4 Implementation of the backprojection and the Barber-Brown filter

This section contains a description of the numerical implementation of the backprojection discussed in the previous section, including a brief description of the spatially dependent filter, which is used to improve the reconstruction.

Let x^b denote the point $x^b = x(s, 1/2, \omega)$ on the boundary of the unit circle obtained by solving

$$U(x, \omega) = s, \quad \text{with} \quad |x| = 1, \tag{25}$$

for a specified s and ω. The data based on which we seek to reconstruct $\delta\gamma$ is

$$W(s, \omega) := -\frac{\partial}{\partial \tau}\delta U / \frac{\partial}{\partial \tau} U(x_b, \omega).$$

The backprojection formula (8) amounts to

$$\tilde{B}(x) = \frac{1}{2\pi}\int_{|\omega|=1} W(s, \omega)|_{s=U(x,\omega)}(2V(x, \omega) - 1)dS_\omega.$$

The discrete approximation to the back projection is represented by a matrix, for simplicity also denoted $\tilde{B}$. For the iterative scheme we will need the entire matrix $\tilde{B}$ not just its action on individual vectors.

We assume that the experimental setup contains m electrodes. The midpoints between electrodes are numbered 1 through m (see Figure 2). A pair of adjacent electrodes through which input current flows (in and out respectively) is called the driver pair. As a realization of a dipole at location 1, we select the driver pair to be the two electrodes adjacent to location 1. We measure voltage differences on all electrode adjacent pairs. The rescaled values of these differences represent our discrete data corresponding to a dipole at location 1. As pointed out by Barber and Brown it is often not possible to obtain reliable values of the voltage tangential derivatives at the dipole location, and the locations adjacent to it (in this illustration, locations 1, 2 and m). This is because measurements of voltages at the driver pair tend to be inaccurate. They suggest filling this data gap by extrapolation from neighboring measurements. In our numerical simulation, we assume that the tangential derivatives of the voltage have been obtained at locations adjacent to the dipole location, and use the fact that the quantity W in the limit of a perfect dipole is zero at the dipole location (see (22)). To obtain the complete data set, we cycle through all possible driver pairs.

The integral above is replaced by a sum over all driver pairs. Thus the discrete version of the backprojection is

$$\frac{1}{m}\sum_{j=1,m} W(s, \omega_j)|_{s=U(x,\omega_j)}(2V(x, \omega_j) - 1). \tag{26}$$

Notice that the point x^b on the boundary, which satisfy (25) for $s = U(x, \omega_j)$ may not lie at a measurement point. Hence interpolation of the data may be necessary.

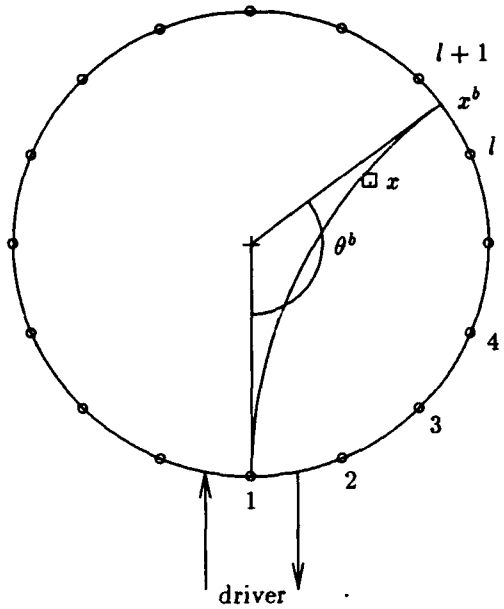

Figure 2 The pixel being illuminated has index i with corresponding location x. The driver electrodes are the pair adjacent to 1. This experiment generates a dipole at 1. Collected measurements at the numbered locations produce the data $\{w_1, w_2, w_3, \cdots\}_{dipole\ at\ 1}$. The equipotential through x intersects the boundary at x^b at angle θ^b. The indices of the electrodes nearest x^b are l and $l+1$.

To represent the data discretely, we use an m^2 vector w. The index on w locates a dipole and a point on the circle at which the tangential derivative of the potential is measured. The value at that index represents the quantity W. The vector w consists of m m-vectors. Each vector corresponds to one experiment, that is, it contains the ratios between the measured tangential derivatives and reference tangential derivatives at all measurement locations for a fixed dipole. Thus

$$w = [(w_1, w_2, w_3, \ldots)_{dipole\ at\ 1}, (w_1, w_2, w_3, \ldots)_{dipole\ at\ 2}, (\ldots)_{dipole\ at\ 3}, \cdots].$$

The original circular domain, $|x| \leq 1$, is embedded into $[-1,1]\times[-1,1]$ for convenience of graphics. The extended domain, which we call the image domain, is discretized so that there are n^2 pixels of size $2/n$ by $2/n$. The conductivity perturbation $\delta\gamma(x)$ is replaced by an n^2 vector, for simplicity also denoted by $\delta\gamma$. The index on the vector $\delta\gamma$ locates a pixel in the image domain, and the value at that index represents the conductivity increment at the center of the pixel.

The backprojection matrix $\tilde{B}$ takes a vector in $\mathbb{R}^{m^2}$ and maps it to $\mathbb{R}^{n^2}$. The row vectors of $\tilde{B}$ which correspond to pixels outside of $|x| \leq 1$ are set to zero. We compute the matrix $\tilde{B}$ by rows. To describe the computation of $\tilde{B}$, let us take a pixel indexed by i, centered at x. The procedure outlined below is based on formula (26).

For illustrative purposes, let us take the case when the dipole is located at index $j = 1$. With this dipole location, we can calculate the first m-entries of the ith row of $\tilde{B}$. Our computational experience, as well as that of Barber and Brown, suggests that a certain smoothing is required. This smoothing is accomplished by imaging several points x^k, neighboring x, and then replacing the terms $W(s,\omega_j)|_{s=U(x,\omega_j)}$ in (26) by the respective averages over the points x^k. As a common weight we use the value of $(2V-1)/m$ at the point x.

At x^k, we have

$$U^k = x_1^k/((x_1^k)^2 + (x_2^k + 1)^2),$$
$$V^k = (x_2^k + 1)/((x_1^k)^2 + (x_2^k + 1)^2).$$

The weight at x is

$$wt = \frac{1}{2\pi}\left(\frac{2(x_2 + 1)}{x_1^2 + (x_2 + 1)^2} - 1\right)$$

A quick calculation shows that the equipotential arc connecting the dipole location 1 and x^k intersects the circular boundary at

$$x_1^b = 4U^k/(4(U^k)^2 + 1),$$

$$x_2^b = 2/(4(U^k)^2 + 1) - 1.$$

From this, we calculate the angle θ^b to be

$$\theta^b = tan^{-1}(-x_1^b/x_2^b).$$

It is now simple to identify the indices l and $l + 1$ corresponding to measurement locations between which the point x^b lies. Linear interpolation gives factors

$$f_l = (\theta_b - \theta_l)/\Delta\theta,$$

$$f_{l+1} = (\theta_{l+1} - \theta_b)/\Delta\theta,$$

corresponding to l and $l + 1$ respectively.

In summary our algorithm for constructing the first m entries of the ith row of the matrix $\tilde{B}$ is:

1) for each point x^k
   a. initialize the m-vector $work^k$ to zero
   b. compute θ^b and identify indices l and $l + 1$
   c. in the vector $work^k$ set the lth and the l+1th entries to f_l and f_{l+1} respectively
2) form the average of all the vectors $work^k$ and store result in the vector $work$
3) calculate the weight wt and multiply $work$ by wt

The resulting vector comprises the first m entries of the ith row of $\tilde{B}$. The scalar multiplication of this row vector with the first m entries of a data vector w is the contribution of the (averaged) operation (26) for $j = 1$ at the image point i. To find the next m entries, move the dipole to location 2 and carry out the same calculation.

In our implementation, we take $m = n = 16$. However, in order to obtain an accurate $\tilde{B}$, we initially calculate it for $m = 64$. The resulting matrix is postmultiplied with an interpolation matrix such as to make $\tilde{B}$ a 256×256 matrix. The interpolation is linear. To achieve a desirable level of smoothing, we take 25 points x^k; these points make up a regular stencil covering an area the size of the pixel centered at x.

The matrix $\tilde{B}$ was used in Barber and Brown [3] to reconstruct point images at various positions in the circle. It was noted that the reconstruction had limited resolution, and it was also noted that the resolution depended on the position. In order to focus the recovered image, they designed a position dependent filter. The construction of this filter is purely heuristic, and some of the parameters are arrived at by experimentation. However, we cannot overlook its effectiveness and so we have included it in our implementation.

Briefly described the filter works as follows: for a fixed pixel at location x one constructs a combination of a rotation and a conformal map in order to map the unit ball to itself and map x to the origin (the rotation takes x to $|x|$ on the positive real axis, the conformal map is now $z \to (z - |x|)/(1 - z\,|x|)$, using the natural identification of $\mathbb{R}^2$ and $\mathbb{C}$). In the new copy of the unit ball one computes the effect of convolution of the transformed $\tilde{B}w$-values with a Gaussian distribution centered at the origin (one actually only computes the convolution at the origin, the point which corresponds to location x). Finally the filtered $\tilde{B}w$-value at the location x is taken to be $c_1 \cdot$(original $\tilde{B}w$-value)$-c_2 \cdot$convolution. The constants c_1 and c_2 are empirically chosen to be 16 and 15 respectively! For more details we refer the reader to [3].

We used Barber and Brown's code without changes to calculate this filter matrix, which we denote by F. The premultiplication of $\tilde{B}$ by F gives what we call the filtered Barber-Brown backprojection, denoted here by

$$B = F\tilde{B}.$$

Thus given a data vector w, corresponding to an experiment, we find a rough reconstruction through $\delta\gamma \approx Bw$. Numerous simulated reconstructions using the matrix B can be found in [3].

5 Properties of the conductivity-to-data map and preconditioning

The forward map, which takes conductivity perturbations $\delta\gamma$ to voltage data w through the approximate solution of (3) will be denoted by E. With the discretization described previously, this map is an $m^2 \times n^2$ matrix, operating on an n^2-vector $\delta\gamma$ to produce an m^2-vector w. To construct this matrix, we use the Green's function discussed in Section 3 and numerical quadrature.

With this notation, the inverse problem we wish to solve can be stated as a system of linear equations in $\delta\gamma$

$$E\,\delta\gamma = w. \tag{27}$$

Here, the vector w is the measured (or synthetic) data.

Numerical results reported in [3], and our own experimentations with the filtered Barber-Brown backprojection on synthetic data, lead us to believe that B is a crude approximate inverse to E. Thus we are led to consider an alternate problem

$$BE\,\delta\gamma = Bw. \tag{28}$$

How well one can solve (27) and (28) depends on the properties of E and BE, and the method employed for the solution. We are ultimately interested in solving the full nonlinear problem described in Section 2. A reasonable approach to such a problem is to use a Gauss-Newton method, where at each step, we need to solve a linear system very much like (27). However, this step is necessary only to obtain an update towards the final solution. Thus in the early stages of the Gauss-Newton method it is often sufficient to solve the resulting linear system only *approximately* (cf. [7]). With this in mind, we rule out direct methods for the solution of (27) and (28), and consider only iterative methods. Of particular interest are conjugate direction algorithms [12], which we expect will yield a good approximate solutions to (27) and (28) in a small number of iterations.

Since E will not in general be square, it is natural to consider the normal equation

$$E^T E\,\delta\gamma = E^T w \tag{29}$$

in order to use a conjugate direction method. We could in principle use an algorithm of Hestenes [13] which avoids forming the normal matrix explicitly. However, regardless of the choice of the algorithm the problem solved is that of equation (29). The conditioning of this solution procedure (convergence rate of the iterations and sensitivity of the solution to noise in the data) depends on the eigenvalues of $E^T E$.

Consider now the problem (28). BE is a square matrix of order n^2, but it is of course not symmetric, which leads to difficulties with many conjugate direction methods. The conjugate residual method (CR) is a special example of a conjugate direction method which is guaranteed to converge for any square system, provided the matrix has definite symmetric part. As will be seen later, the symmetric part of BE is not exactly definite, however nearly all of its large eigenvalues have same sign (positive). In practice this should insure that conjugate residual applied to BE will converge for a wide range of initial guesses. From the point of view of computation, this method is advantageous because it works on the matrix BE and not the matrix $(BE)^T BE$. The eigenvalues of BE may be viewed as determining the conditioning of this solution procedure [9].

We are only interested in the action of E and BE on vectors corresponding to images contained in the unit circle. Therefore we remove columns of E, and columns and rows of BE corresponding to pixels lying outside the unit circle.

For $m = n = 16$ we have 256 pixels of which only 208 corresponds to locations inside the circle. We computed the eigenvalues of the symmetric part of the matrix BE and found that of the the moderate to large size eigenvalues, all except for one are *positive* (see Figure 3a). The eigenvector corresponding to the negative eigenvalue is displayed in Figure 3b and seems to represent a constant background with perturbations near the boundary. The difficulties posed to the conjugate residual method by the presence of this "bad" direction can be avoided if one restricts $\delta\gamma$ to be supported sufficiently far away from the boundary.

In contrast, the symmetric part of E has about equally many large positive and large negative eigenvalues. This explains why even in the square case we cannot apply conjugate residual successfully to E alone.

As pointed out earlier, we believe that the eigenvalues of $E^T E$ and BE provide information about the conditioning of our solution procedures for problems (27) and (28) respectively. The eigenvalues of $E^T E$ are displayed in Figure 4. The fact that the eigenvalues beyond the 62th are all less than 10^{-3} reflects the illposedness of the problem. The largest eigenvalue is 1.958. The moduli of the eigenvalues of BE are shown in Figure 5 (BE, being nonsymmetric, has some small complex eigenvalues starting with the 73rd). We find that the conditioning is somewhat better here; the largest modulus of any eigenvalue is 1.080 and eigenvalues whose moduli are less than 10^{-3} begin with the 87th. The tapering off of the eigenvalues in both cases indicates that some resolution loss in reconstructing $\delta\gamma$ is inevitable.

Let g_j denote the eigenvectors of $E^T E$, with the corresponding eigenvalues in descending order. The iterates of conjugate direction algorithms in practice often appear to be related to projections of the true solution onto the span of $\{g_j\}_{j=1,\cdots,J}$ for increasing J. Therefore it is instructive to consider the projections of a fixed vector onto the span of $\{g_j\}_{j=1,\cdots,J}$. Let h_j denote the eigenvectors of BE. We also consider the projections of the same fixed vector onto the span of $\{h_j\}_{j=1,\cdots,J}$.

We take a profile whose entries are zero except for one corresponding to the pixel whose midpoint is (0.0625, 0.0625). We project this profile onto the space spanned by the $\{g_j\}_{j=1,\cdots,J}$ for $J = 30$ and $J = 100$. The results are shown in Figures 6a and 6b.

It is not clear if any iterative method will get as far as $J = 100$ because the 100th

eigenvalue of $E^T E$ is of the order 10^{-7}. In some sense Figure 6b gives an indication of the the minimal resolution loss to be expected. Notice that with $J = 30$, the projected image is very far from the point profile. Indeed the Barber-Brown method produces a superior image using noiseless synthetic data generated from the point profile (compare Figure 6a and Figure 7). There are two eigenvalues of BE with nonzero imaginary part among the first 100 (the conjugate pair corresponds to number 73 and 74). The projection of any real vector onto $\{h_j\}_{j=1,\cdots,J}, J \leq 100$, must therefore be real except for $J = 73$. We project the same point profile as before onto the space spanned by $\{h_j\}_{j=1,\cdots,J}$ for $J = 30, 100$. In both cases the projected image is superior to the projected image using the eigenvectors of $E^T E$. (compare Figure 6 with Figure 8).

We believe that this numerical study indicates that the iterates of CR for equation (28) will converge faster and ultimately get closer to the a consistent profile than the iterates of CR when applied to the normal equation (29).

To separate the effects of the filter from the backprojection, we also computed the eigenvalues of the symmetric part of $\tilde{B}E$. We found that the eigenvalues are similar in structure to those of the symmetric part of BE (only one large negative eigenvalue). The presence of the filter does however increase the size of the eigenvalues.

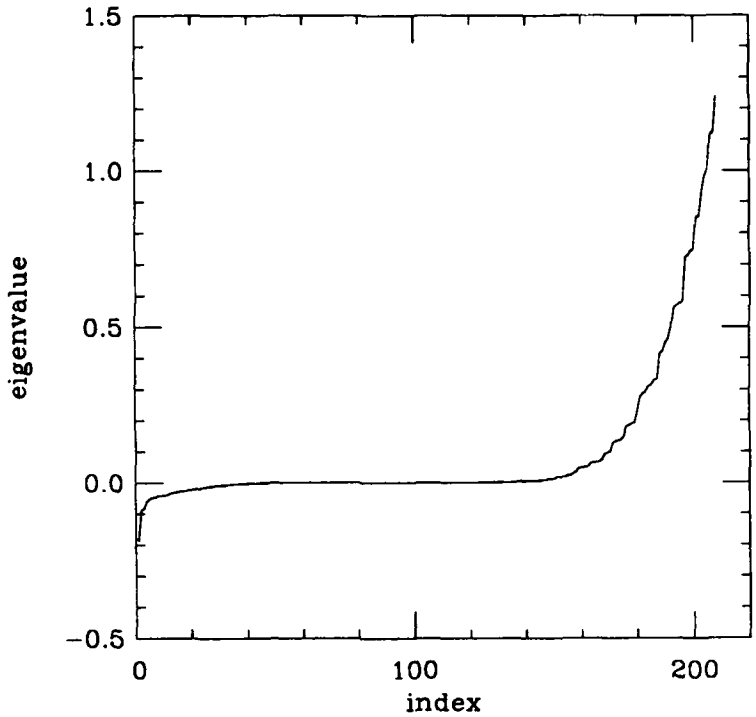

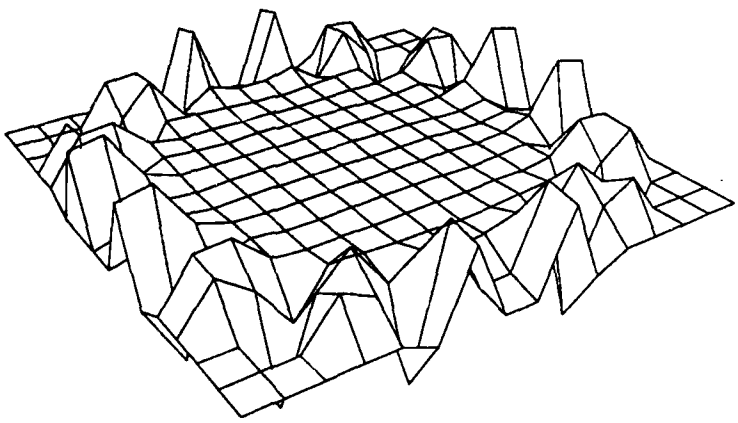

Figure 3 (a) The eigenvalue distribution of the symmetric part of the matrix BE. (b) The eigenvector corresponding to the single large negative eigenvalue.

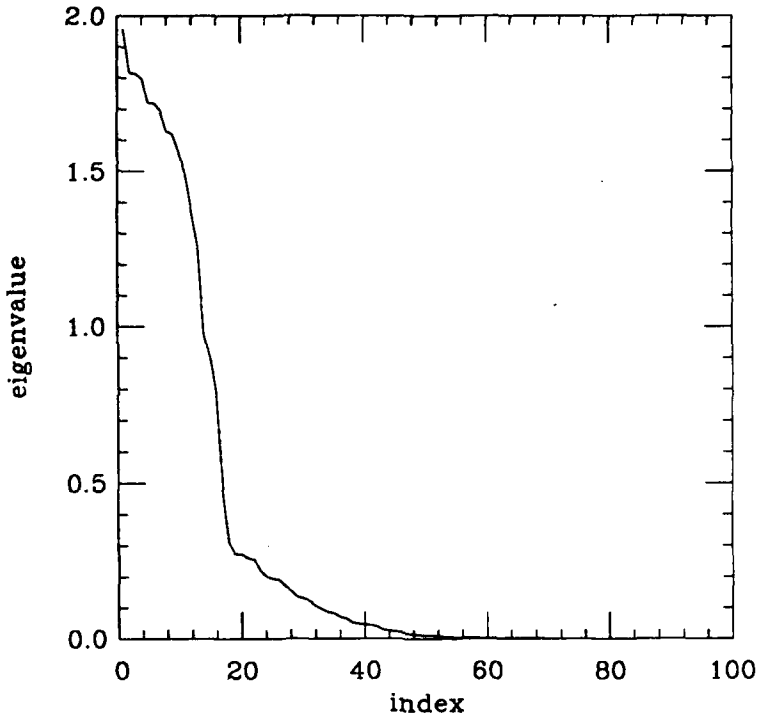

Figure 4 Plot of the distribution of the eigenvalues of $E^T E$. The largest eigenvalue is 1.958, and the eigenvalues beyond the 62nd are less than 10^{-3}.

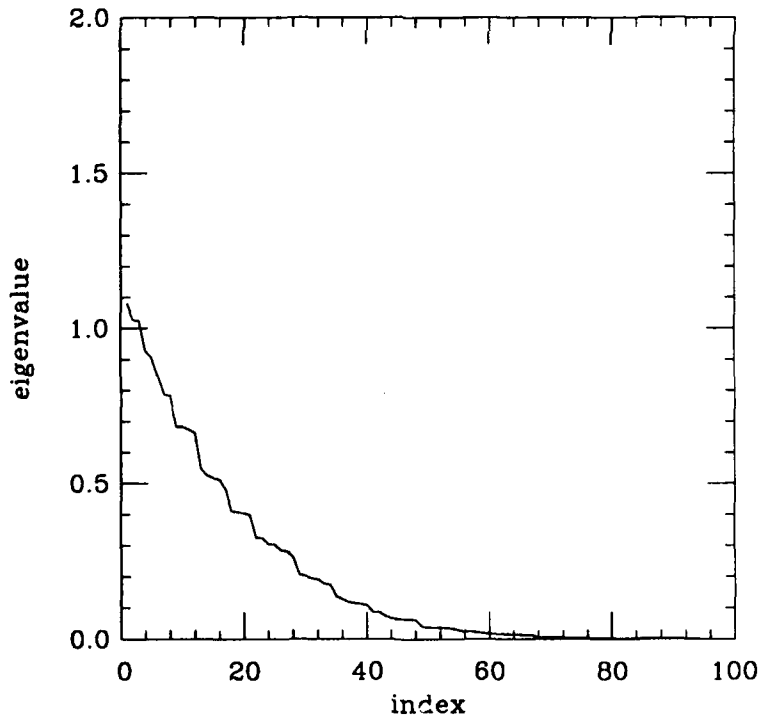

Figure 5 Plot of the distribution of the moduli of the eigenvalues of BE. The largest modulus is 1.080, and the eigenvalues beyond the 87th have moduli less than 10^{-3}.

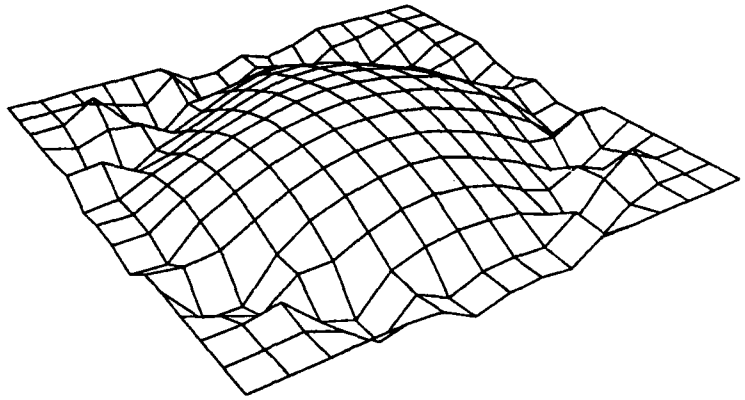

Figure 6a A point image is selected, with all pixels zero except at location $(0.0625, 0.0625)$ which has value 1. This image is projected onto the span $\{g_j, j = 1, \ldots, 30\}$. The eigenvalues have been arranged in descending order, g_j is the jth eigenvectors of $E^T E$. The maximal value of the projection is 0.0213, the minimal value is -0.0170.

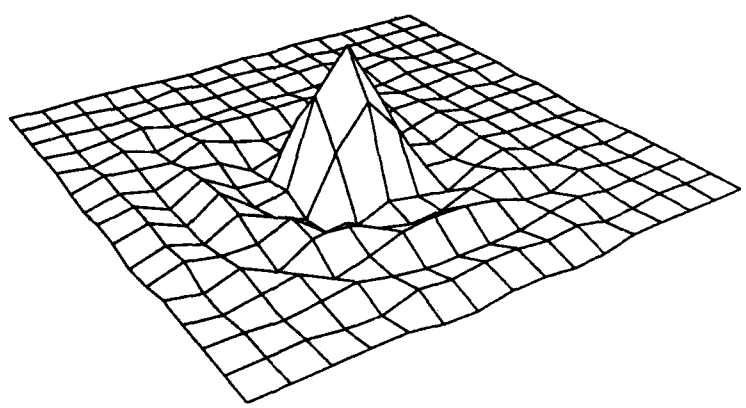

Figure 6b Projection of the same point image as used in Figure 6a onto the span $\{g_j, j = 1, \ldots, 100\}$. Maximal value = 0.2970, minimal value = -0.0522.

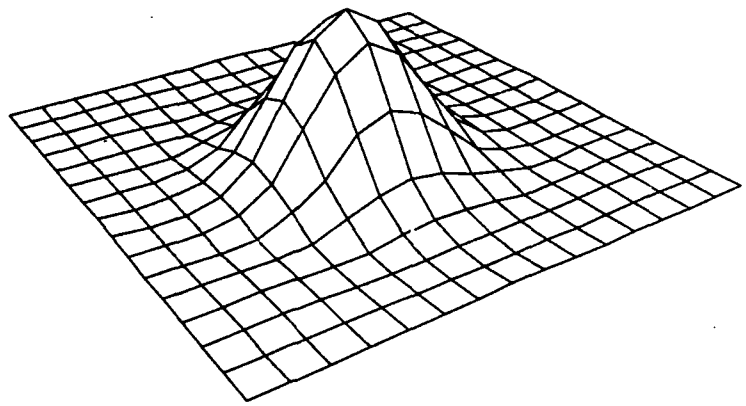

Figure 7 The Barber-Brown reconstruction of the same point image as used in Figure 6 based on simulated data. Maximal value = 0.0623, minimal value = -0.0015.

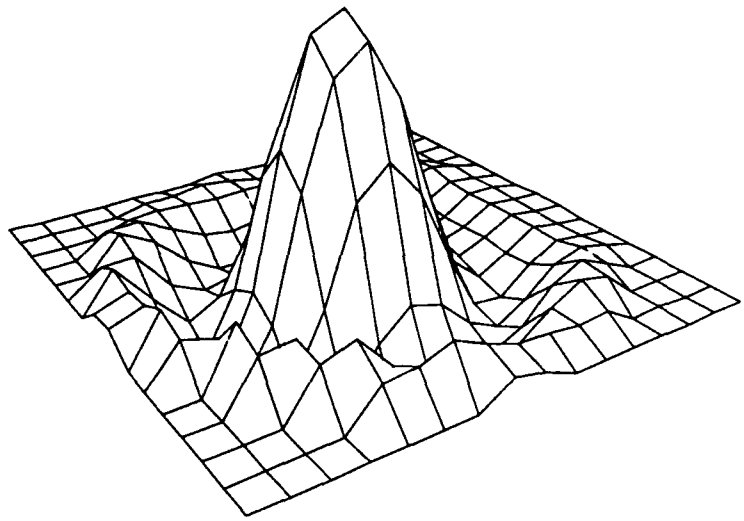

Figure 8a Projection of the same point image as used in Figure 6 onto the span $\{h_j, j = 1, \ldots, 30\}$. Compare to Figure 6a. Maximal value = 0.1033, minimal value = -0.0254.

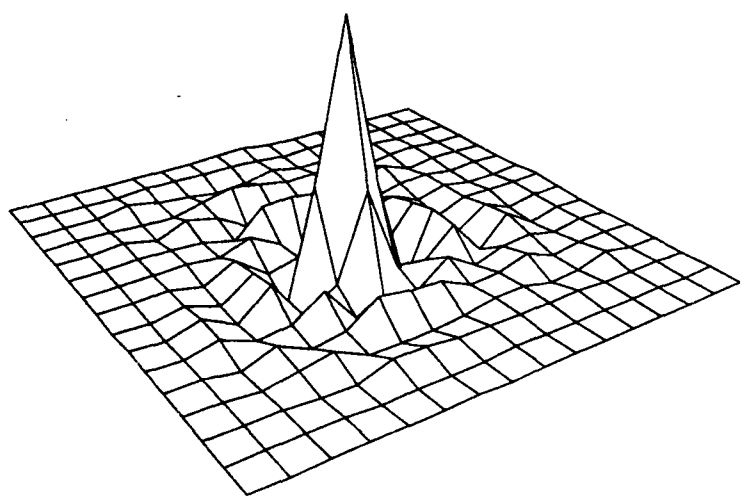

Figure 8b Projection of the same point image as used in Figure 6 onto the span $\{h_j, j = 1, \ldots, 100\}$. Compare to Figure 6b. Maximal value = 0.5715, minimal value = -0.1105.

6 An iterative refinement for the reconstruction

The conjugate residual method [8, 9] solves the following linear equation:

$$Ax = f,$$

where A is a square, but possibly nonsymmetric, matrix of order N with definite symmetric part. Suppose the initial guess is x_0 and the initial residual is $r_0 = f - Ax_0$. The iterates x_i are ideally obtained by minimizing

$$||Ax_i - f||$$

over the translated Krylov space

$$x_0 + \{r_0, Ar_0, \cdots, A^{i-1}r_0\}.$$

The minimization is performed by consecutive line searches in directions that satisfy the conjugacy conditions

$$(Ap_j, Ap_i) = 0, \quad \text{for} \quad j \neq i.$$

In practice, for a nonsymmetric matrix A, one does rarely satisfy all the conjugacy conditions above. The version of the algorithm we have implemented in general only guarantees that $(Ap_{i-1}, Ap_i) = 0$. This version is:

(i) choose an initial guess x_0.

(ii) compute the initial residual $r_0 = f - A\,x_0$.

(iii) set search direction $p_0 = r_0$.

(iv) for $i = 0$ step 1 until convergence do

- (a) $a_i = (r_i, Ap_i)/(Ap_i, Ap_i)$
- (b) $x_{i+1} = x_i + a_i p_i$
- (c) $r_{i+1} = r_i - a_i Ap_i$
- (d) $b_i = -(Ar_{i+1}, Ap_i)/(Ap_i, Ap_i)$
- (e) $p_{i+1} = r_{i+1} + b_i p_i$

Although this version of the conjugate residual method does not guarantee that all the conjugacy conditions $(Ap_j, Ap_i) = 0$, $j \neq i$, are satisfied, and therefore in general does not give iterates which minimize the residual over the relevant translated Krylov spaces, this version is known to converge when applied to matrices with definite symmetric part. We refer the reader to [8, 9] for a detailed analysis.

For the solution of (29), we simply set $A = E^T E$, and as the intial guess, we take the filtered Barber-Brown backprojected image.

For images $\delta\gamma$ supported near the boundary, one encounters instabilities by a direct application of CR to (28) with $A = BE$. We see this as a manisfestation of the presence of the "bad" search direction corresponding to the large negative eigenvalue (cf. Figure 3). To eliminate this difficulty, we set to zero all rows and columns of BE corresponding to pixels outside a circle with a priori prescribed radius $r < 1$. In matrix notation, this corresponds to post- and premultiplication with a matrix Π_r obtained from the identity matrix by setting to zero the columns corresponding to pixels outside $r < 1$. In our implementation we apply CR with $A = \Pi_r BE\Pi_r$, for an appropriate choice of r, and we take the filtered Barber-Brown backprojected image as initial guess. If the image $\delta\gamma$ is not supported near the boundary, one may use $r = 1$ without any difficulty. If r is accidentally chosen too small, it is quite easily recognized by the failure of the residuals to become small.

7 Numerical experiments

We conclude this paper with some numerical results. In Section 5, we made a prediction that of the two problems,

$$E^T E\, \delta\gamma = E^T w \qquad (P1)$$

$$BE\, \delta\gamma = Bw, \qquad (P2)$$

the latter is more well-behaved. By this we meant that the iterates of the CR algorithm applied to equation (P2) should converge faster and ultimately get closer to a consistent profile than iterates of the same CR algorithm applied to (P1).

To verify our prediction we show the results of computations with two representative test profiles. In both cases the data is generated by a multiplication of the test profile by the matrix E, i.e., by modeling perfect dipoles at the numbered locations in Figure 2, and solving the perturbational equations (3) through the use of the Green's function and numerical quadrature. The data is in the range of E and noiseless (to roundoff errors).

In our first test the profile used is shown in Figure 9a. The profile represents a ring-shaped high conductivity perturbation with a ridge across (the ridge has only half the strength of the outer ring). The ring is not circular, its thickness varies and it is off center. In Figure 10a we display the relative problem residual

$$||E\, \delta\gamma_i - w||/||w||$$

versus number of iterations of the CR algorithm for both equation (P1) and (P2). $||\ ||$ denotes the Euclidian norm. It is clear that the residuals in the case of (P2) are smaller than in the case of (P1) (by about a factor of 1/2 at the 30th iterate). This is also reflected in how well the iterates match the "correct" profile $\delta\gamma$. In Figure 10b we display the relative error

$$||\delta\gamma_i - \delta\gamma||/||\delta\gamma||,$$

versus number of iterations of the CR algorithm for both equations (P1) and (P2). At the 30th iterate the error in the case of equation (P1) is about 41% where as in the case of equation (F2) this has been reduced to around 23% (a slightly smaller reduction than for the residuals). Most impressive to observe is how much faster the CR iterates for (P2) converge during the first 6 steps when compared to those for (P1).

For further comparison we examine the reconstructed profiles at the 30th iteration. For reference we show the filtered Barber-Brown backprojection (initial guess for the iterative schemes) in Figure 9b. The 30th iterates for (P1) and (P2) are show in Figures 9c and 9e respectively. Notice that the ridge is recovered in the case of (P2) while it is still not visible in the case of (P1). In fact the ridge begins to be visible in the 5th CR iterate of (P2). Figures 9d and 9f are greylevel plots of the same profiles shown in Figures 9c and 9e respectively. The ridge is clearly visible in 9f whereas it is not seen at all in 9e. In the computations of the CR iterates for (P2) we used a cutoff radius of $r = 0.85$ to avoid instabilities, as described in the last part of Section 6.

Our second test involves a profile in the form of two rings, one twice as high as the other, as shown in Figure 11a. We display the relative problem residual (Figure 12a) and the relative error (Figure 12b) versus the iteration number. Again the CR iterates for (P2) perform significantly better than those for (P1), especially in the first few steps. Figures 11b, 11c and 11e show the filtered Barber-Brown backprojection, the 30th iterate of CR applied to (P1) and the 30th iterate of CR applied to (P2). Figures 11d and 11f are the greylevel plots of the profiles shown in Figures 11c and 11e. Notice that the holes (the areas of low conductivity inside the rings) are recovered in the case of (P2) (in fact they are already visible in the 7th iterate), while they are still invisible in the case of (P1). Since this profile is supported further away from the boundary than the profile

used in the first test no cutoff is necessary in the computations related to (P2) (cf. the end of Section 6).

These two tests, and several others we have performed, indicate that B acts as a reasonably good preconditioner for the original problem. It is fortunate that BE is positive definite except for a single (controllable) direction. This allows us to use CR on (P2). It remains to be seen whether BE retains the same property when E corresponds to a background conductivity which is not constant. If this were the case, then we can construct a relatively efficient and accurate scheme for the full nonlinear problem (compared to output leastsquares).

In summary we conclude that the CR algorithm applied to the equation $BE\delta\gamma = Bw$ gives an iterative method which

1) allows us to significantly improve upon the filtered Barber-Brown backprojection,

2) performs better than the conjugate gradient or the conjugate residual algorithm applied to the normal equation $E^T E\delta\gamma = E^T w$

(since the matrix $E^T E$ is symmetric and positive definite, the conjugate gradient and the conjugate residual algorithms will behave similarly). We are hopeful that the same result may be obtained for much more general domains.

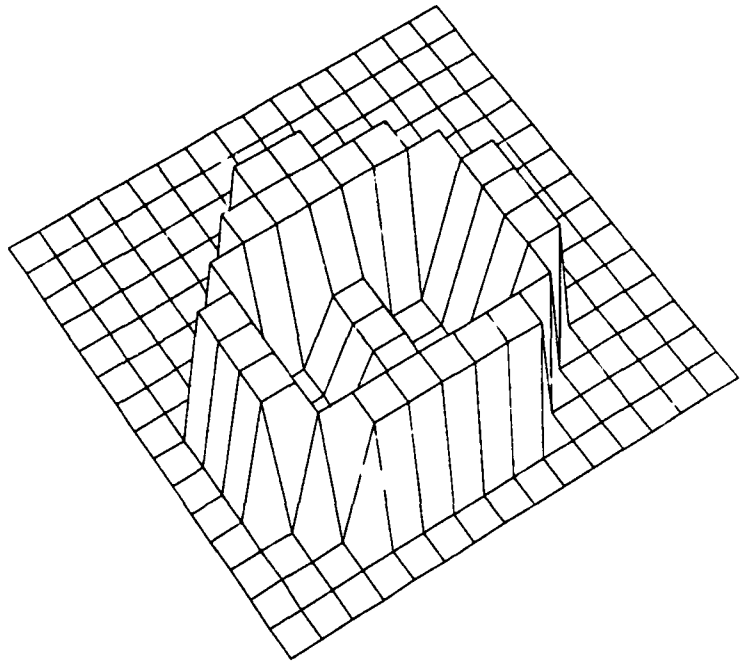

Figure 9a The test profile

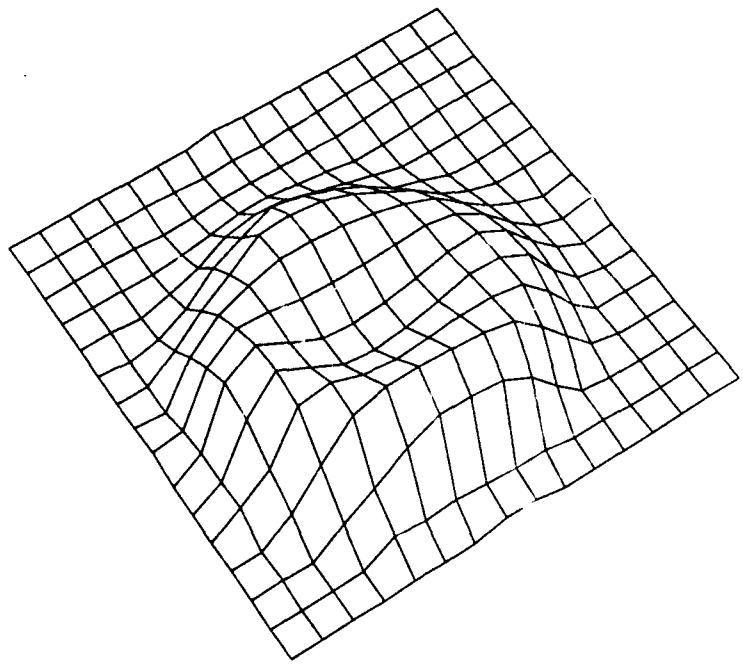

Figure 9b Reconstruction using the filtered Barber-Brown backprojection.

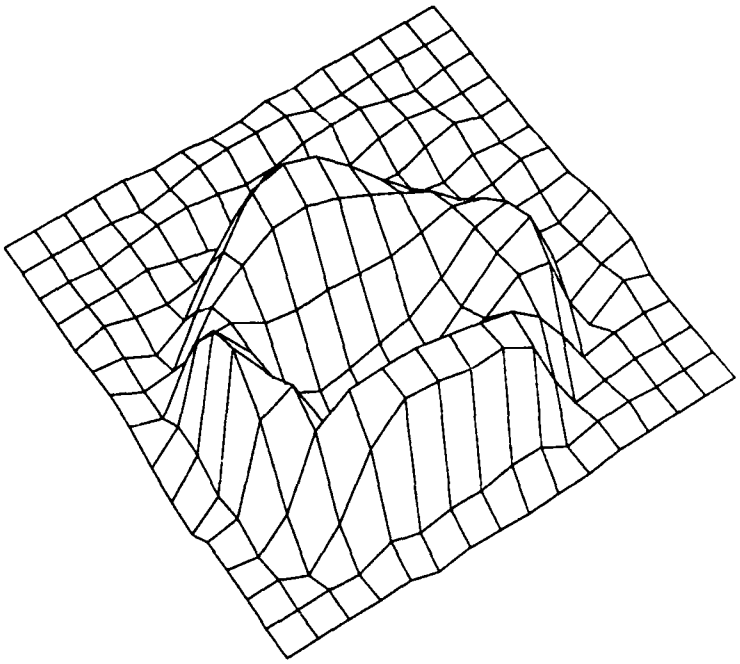

Figure 9c Reconstruction based on (P1) at the 30th iterate of the conjugate residual algorithm.

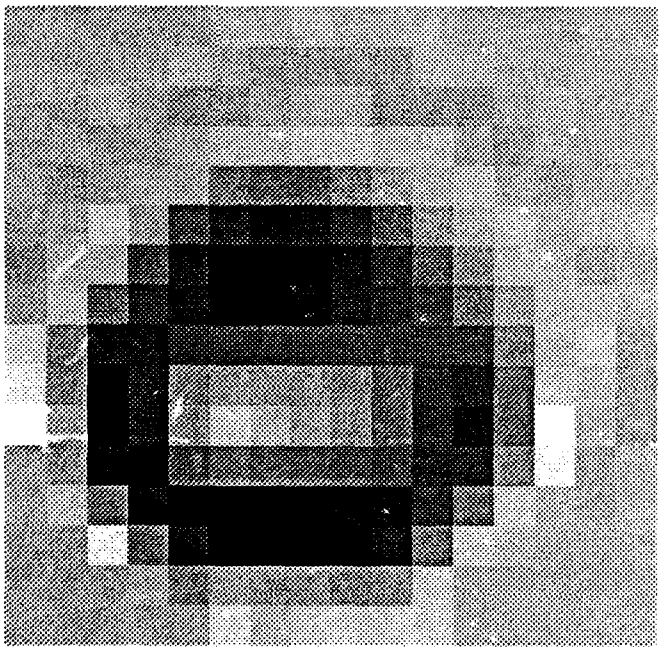

Figure 9d Gray level plot of Figure 9c.

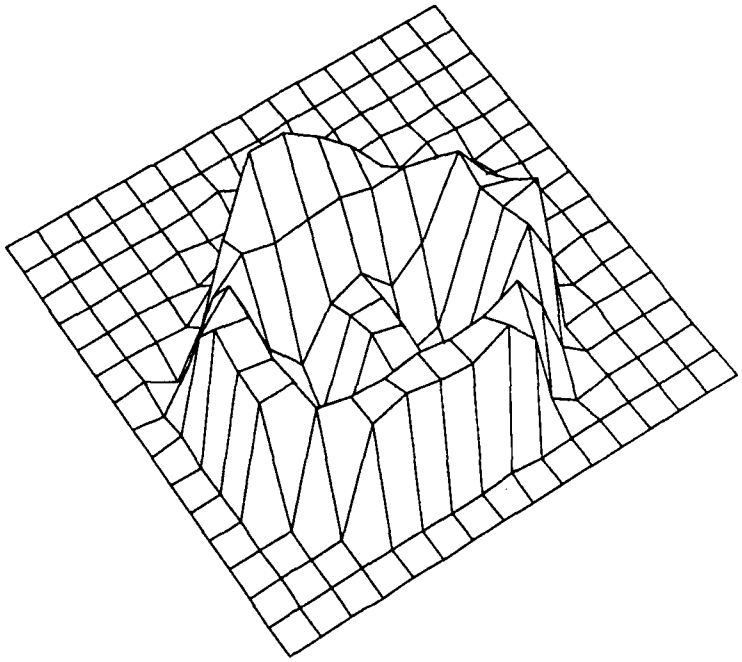

Figure 9e Reconstruction based on (P2) at the 30th iterate of the conjugate residual algorithm.

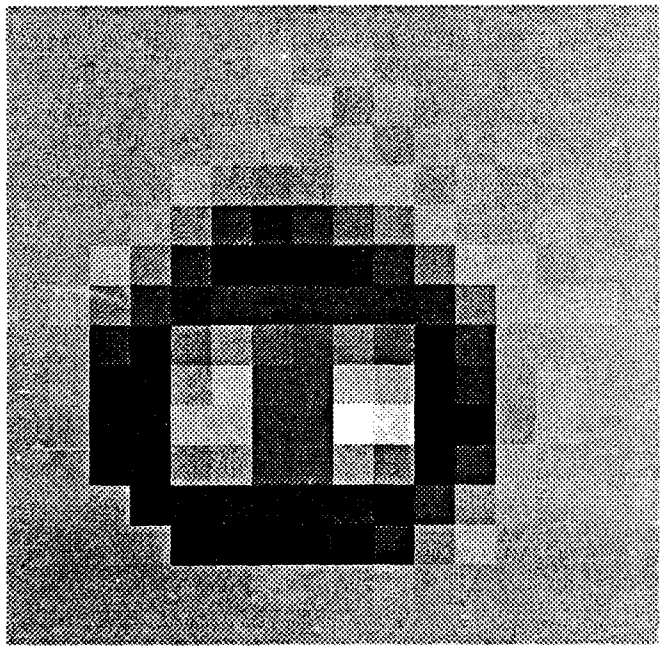

Figure 9f Gray level plot of Figure 9e.

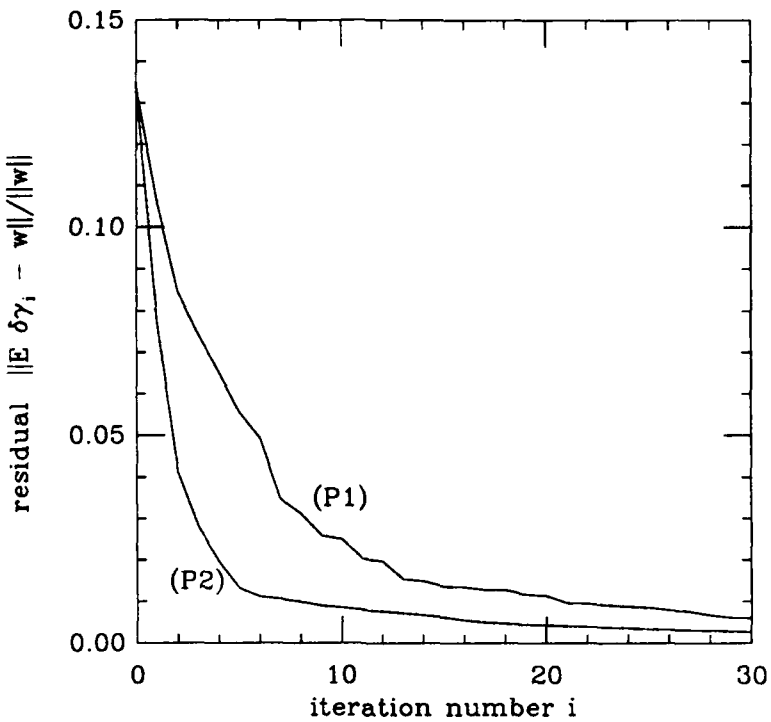

Figure 10a Reduction in the relative problem residual versus number of iterations.

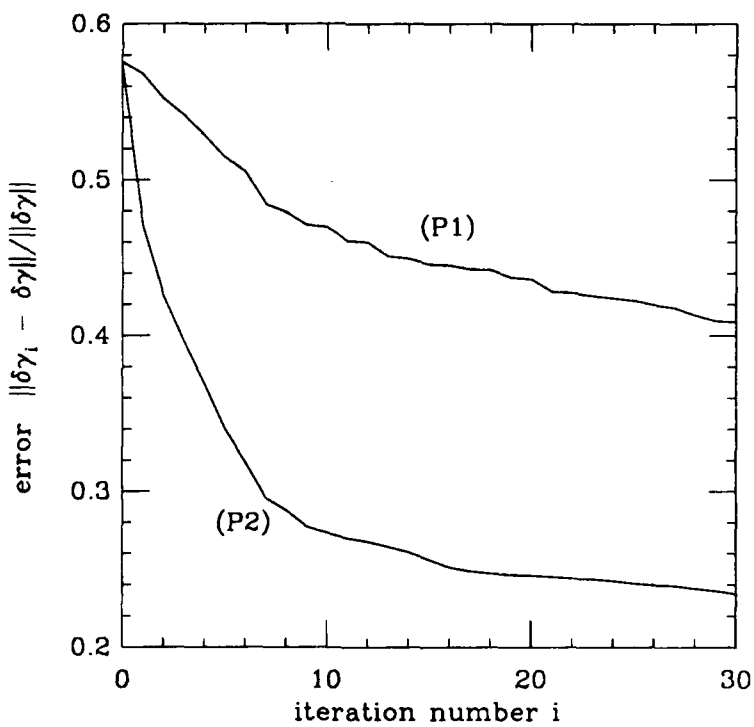

Figure 10b Relative L^2 error in the recovered profile versus number of iterations.

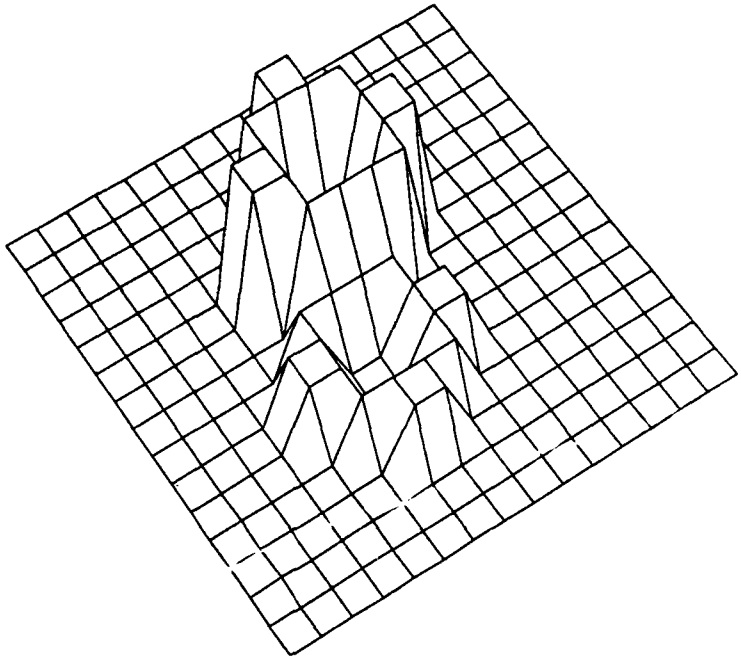

Figure 11a The test profile

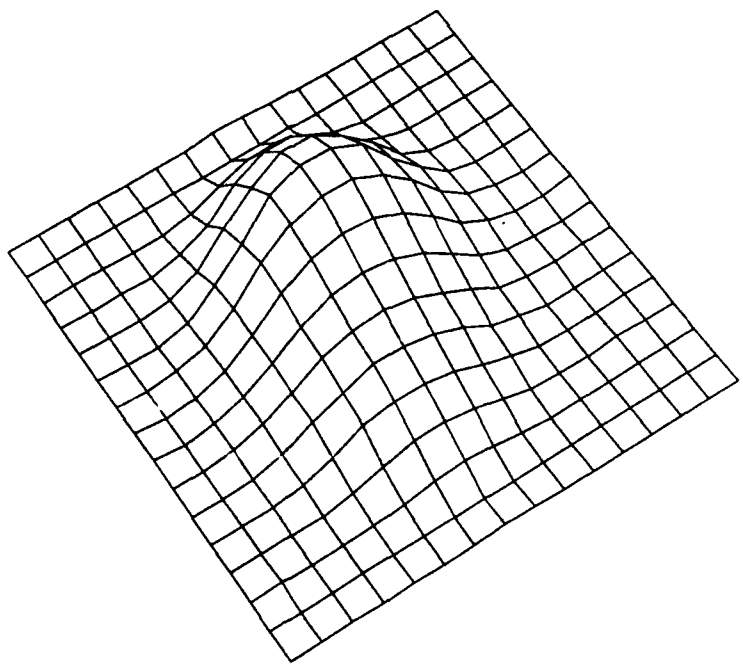

Figure 11b Reconstruction using the filtered Barber-Brown backprojection.

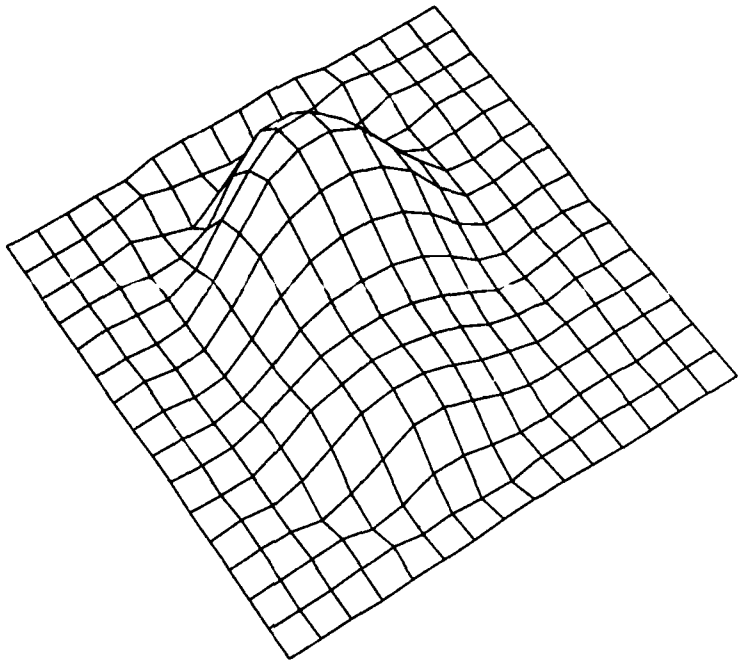

Figure 11c Reconstruction based on (P1) at the 30th iterate of the conjugate residual algorithm.

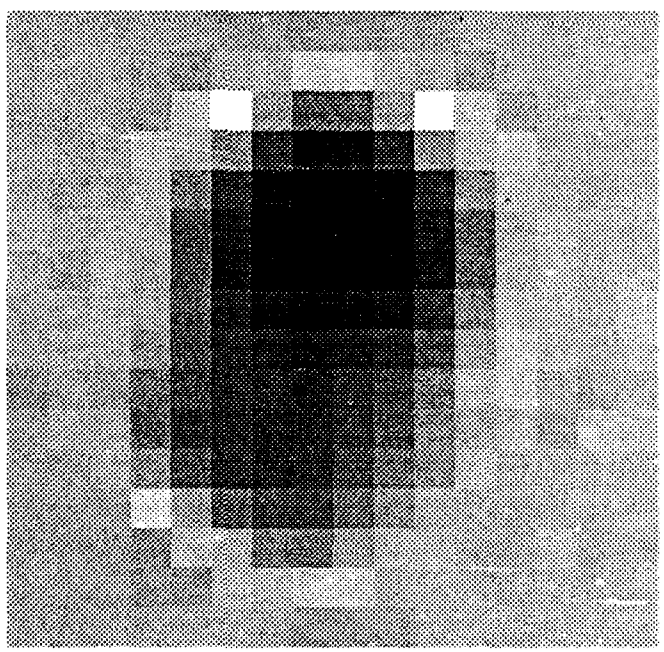

Figure 11d Gray level plot of Figure 11c.

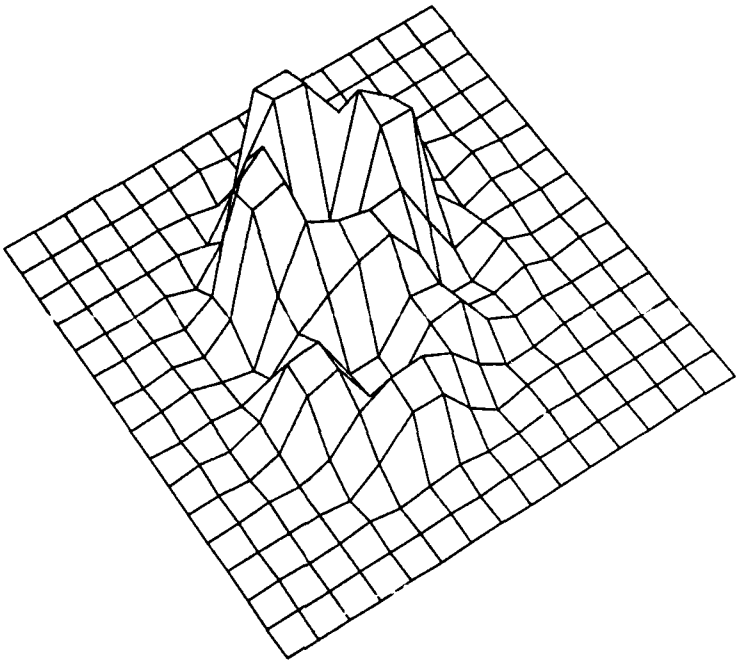

Figure 11e Reconstruction based on (P2) at the 30th iterate of the conjugate residual algorithm.

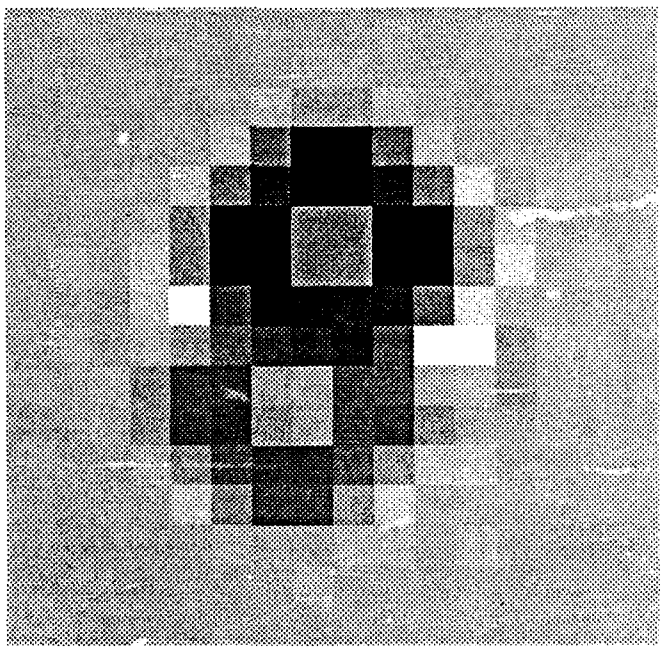

Figure 11f Gray level plot of Figure 11e.

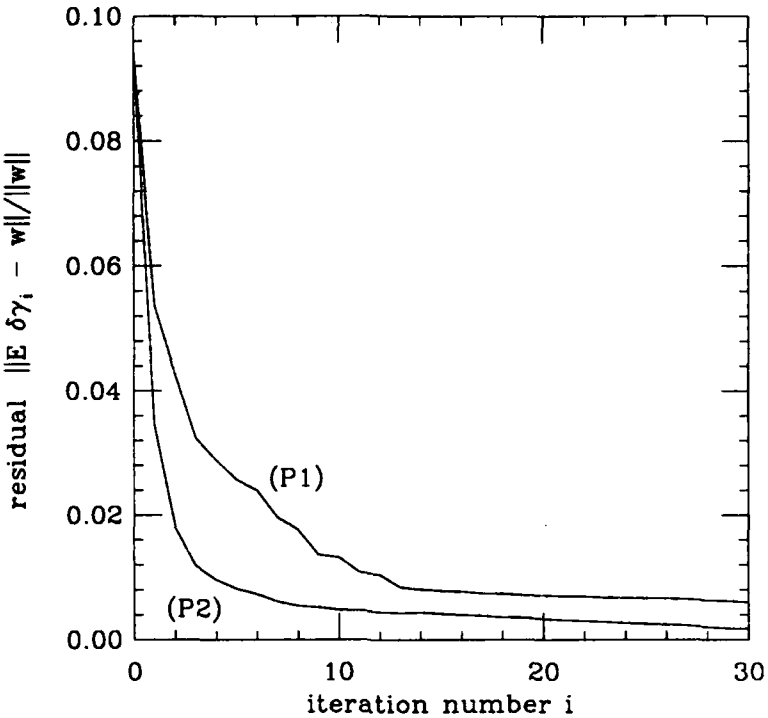

Figure 12a Reduction in the relative problem residual versus number of iterations.

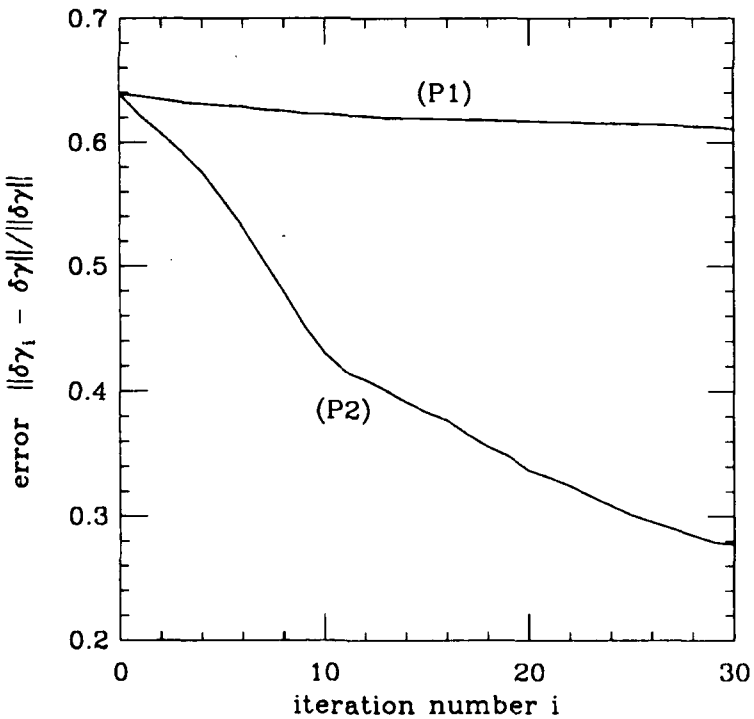

Figure 12b Relative L^2 error in the recovered profile versus number of iterations.

Acknowledgements

The research reported here was completed while Fadil Santosa was a visitor in the Department of Mathematics at the University of Maryland during its special year on numerical analysis 1987-1988. He would like to thank his colleagues in the department for their hospitality. We would like to thank Tom Yorkey for supplying us with a version of the Barber and Brown backprojection code, which was helpful in our own implementation of the method.

List of References

1. Alessandrini, G., Stable determination of conductivity by boundary measurements, IMA Tech. Report 1987.

2. Barber, D. and Brown, B., Applied potential tomography, J. Phys. E: Sci. Instrum., **17** (1984), 723-733.

3. Barber, D. and Brown, B., Recent developments in applied potential tomography - APT, in *Information Processing in Medical Imaging*, S. Bacharach, ed., 106-121, Nijhoff, 1986.

4. Beylkin, G., The inversion problem and applications of the generalized Radon transform, Comm Pure. Appl. Math., **37** (1984), 580-599.

5. Beylkin, G., Imaging of discontinuities in the inverse scattering problem by inversion of a causal generalized Radon transform, J. Math. Phys., **26** (1985), 99-108.

6. Brown, B.H. ed., *Proceedings of the EEC Workshop on Electrical Impedance Imaging*, Sheffield, England, 1986.

7. Dennis, J. and Schnabel, R., *Numerical methods for unconstrained optimization and nonlinear equations*, 1983 Prentice-Hall, Englewood Cliffs, NJ.

8. Eisenstat, S., Elman, H. and Schultz, M., Variational iterative methods for nonsymmetric systems of linear equations, SIAM J. Numer. Anal., **20** (1983), 345-357.

9. Elman, H., Iterative methods for large, sparse, nonsymmetric systems of linear equations, Ph. D. thesis, Yale University, Department of Computer Science, 1982.

10. Friedman, A. and Vogelius, M., Identification of small inhomogeneities of extreme conductivity by boundary measurements: a continuous dependence result, to appear in Arch. Rat. Mech. Anal.

11. Gisser, D., Isaacson, D. and Newell, J., Electric current computed tomography and eigenvalues I, preprint 1987.

12. Golub, G. and Van Loan, C., *Matrix computations*, 1983 The Johns Hopkins University Press, Baltimore, MD.

13. Hestenes, M., Pseudoinverses and conjugate gradients, Comm. ACM, **18** (1975), 40-43.

14. Kohn, R. and Vogelius, M., Determining conductivity by boundary measurements, Comm. Pure Appl. Math., **37** (1984), 289-298.

15. Nachman, A., Reconstruction from boundary measurements, preprint 1987.

16. Seagar, A., Probing with low frequency electric currents, Ph. D. thesis, Univerisity of Canterbury, 1983.

17. Wexler, A., Fry, B. and Neumann, M., Impedance-computed tomography algorithm and system, Applied Optics, **24** (1985), 3985-3992.

18. Sylvester, J. and Uhlman, G., A global uniqueness theorem for an inverse boundary value problem, Annals of Math., **125** (1987), 153-169.

19. Yorkey, T., Webster, J. and Tompkins, W., Comparing reconstruction algorithms for electrical impedance tomography, IEEE Trans. Biomedical Eng., **BME-34** (1987), 843-852.

END
DATE
FILMED
11-88
DTIC